ARTICLE   OPEN

Electron transport and scattering mechanisms in ferromagnetic monolayer Fe$_3$GeTe$_2$

Danis I. Badrtdinov [1 ✉], Georgy V. Pushkarev[2], Mikhail I. Katsnelson [1] and Alexander N. Rudenko [1 ✉]

We study intrinsic charge-carrier scattering mechanisms and determine their contribution to the transport properties of the two-dimensional ferromagnet Fe$_3$GeTe$_2$. We use state-of-the-art first-principles calculations combined with the model approaches to elucidate the role of the electron-phonon and electron-magnon interactions in the electronic transport. Our findings show that the charge carrier scattering in Fe$_3$GeTe$_2$ is dominated by the electron-phonon interaction, while the role of magnetic excitations is marginal. At the same time, the magnetic ordering is shown to effect essentially on the electron-phonon coupling and its temperature dependence. This leads to a sublinear temperature dependence of the electrical resistivity near the Curie temperature, which is in line with experimental observations. The room temperature resistivity is estimated to be ~ 35 $\mu\Omega \cdot$ cm which may be considered as a lower intrinsic limit for monolayer Fe$_3$GeTe$_2$.

INTRODUCTION

The interest to two-dimensional (2D) systems is driven by the continuous progress in the development of novel technologies involving miniaturization of electronic devices and low-energy consumption. A special place in this search is devoted to 2D magnetic materials, which became the subject of active studies after the exfoliation of van der Waaals magnets such as CrI$_3$[1], Cr$_2$Ge$_2$Te$_6$[2], Fe$_3$GeTe$_2$ (FGT)[3–6], etc. Magnetic properties of these systems demonstrate high tunability (e.g. by external electrical field[7] and environmental screening[8]) promising for technological application, as well as serve as an excellent platform for probing the magnetic interactions in low dimensions.

Most of the known 2D magnets are insulating or semiconducting, which limits our understanding of their transport properties and the underlying physical mechanisms. In contrast, FGT has a number of special characteristics since it combines a metallic behavior, needed for the realization of controllable transport[9,10], with the ferromagnetic ground state and comparably high Curie temperature $T_C \simeq$ 220 K[3,4,11], surviving down to the monolayer limit[5]. One of the most remarkable properties of FGT is the absence of inversion symmetry, allowing for the formation of topologically nontrivial magnetic textures[12,13]. A hexagonal lattice of skyrmions is recently observed in this system[14–16], which might be important for spintronics applications. While a considerable attention is paid to skyrmions, the electron transport and scattering mechanisms in FGT remain unclear from the microscopic point of view.

In comparison to nonmagnetic 2D systems, the charge carrier scattering in conductive magnets is not limited to the impurities or phonons, but may include scattering by spin fluctuations[17,18] (Fig. 1b), providing essential contribution to the transport characteristics and/or give rise to qualitatively new effects (e.g., Kondo effect)[19,20]. Moreover, temperature dependence of the spin-polarized electronic structure in magnetically ordered systems might play a role for the conventional sources of scattering (e.g., phonons). The first-principles theory of electron-phonon interactions is well established[21], and has been routinely applied to study transport properties of nonmagnetic 3D and 2D materials[22–26]. Strictly

speaking, a theoretical description of the electron-phonon scattering in 2D is more involved due to the presence of flexural phonon modes[27], allowing for multiple phonon scattering[27–29], yet the single-phonon formulation turns out to be sufficient even for a quantitative description of the charge carrier transport in most of the cases[30]. Generalization of the first-principles scattering theory to magnetic materials is not straightforward for at least two reasons: (i) Unequal and temperature-dependent contribution of the majority and minority electronic states; (ii) The presence of additional scattering channels such as collective spin excitations (magnons) and spin inhomogeneities. Despite a notable progress in this direction being made in recent years, the proposed theories for the first-principles description of electron-magnon interactions [17,31] are limited to zero temperature, i.e. not readily applicable to study transport characteristics. Alternatively, there are well-established theories based on the model description of magnetism[32–34], which are sufficient to capture the corresponding effects qualitatively and, in many cases, quantitatively.

In this work, we perform a systematic study of the charge carrier transport in ferromagnetic monolayer Fe$_3$GeTe$_2$ using first-principles calculations combined with magnetic models. We analyze electron-phonon and electron-magnon scattering, and estimate their contribution to the temperature-dependent scattering rate. The main contribution of the electron-magnon scattering to the resistivity is observed around the Curie temperature, resulting in a marginal resistivity enhancement. On the other hand, interpolation of the electron-phonon scattering between the ferromagnetic and paramagnetic phases leads to a pronounced modification of the resistivity with sublinear temperature dependence close the Curie temperature, which is in line with the experimental observations[4,9,11,35,36].

RESULTS

Electronic structure

Figure 2 shows the electronic structure and Fermi surfaces calculated for monolayer Fe$_3$GeTe$_2$. We explicitly consider electronic

[1]Institute for Molecules and Materials, Radboud University, Heijendaalseweg 135, NL-6525 AJ Nijmegen, The Netherlands. [2]Theoretical Physics and Applied Mathematics Department, Ural Federal University, 620002 Yekaterinburg, Russia. ✉email: d.badrtdinov@science.ru.nl; a.rudenko@science.ru.nl
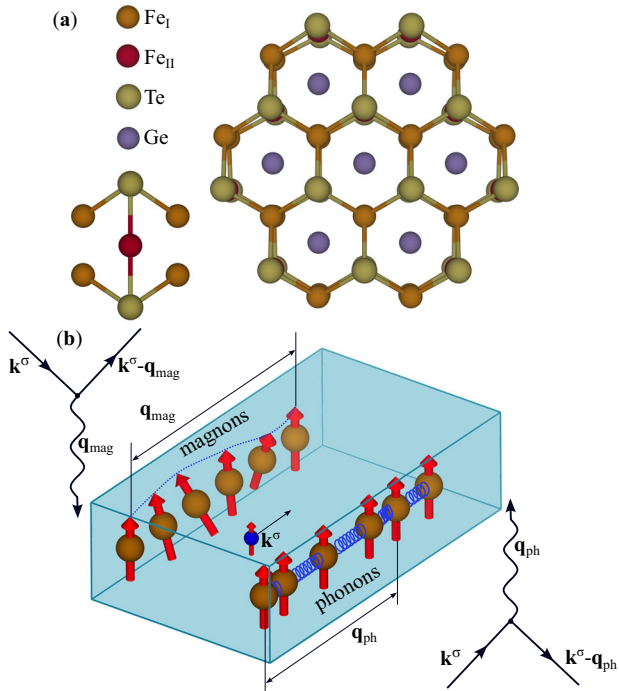
Fig. 1 Schematic crystal structure and main electron scattering mechanisms in monolayer Fe_3GeTe_2. a Crystal structure of Fe_3GeTe_2 with side (left) and top (right) views. Fe_I and Fe_{II} denote two inequivalent iron atoms. **b** A sketch showing scattering of an electron on phonons and magnons.

states in the ferromagnetic (FM) and nonmagnetic phases. The bands in the vicinity of the Fermi energy are predominantly formed by the Fe (3d) states hybridized with Te (5p). The spin-resolved electronic structure in the FM phase displays multiple energy bands crossing the Fermi energy, resulting in the formation of several isolated pockets in the Fermi surface, being in agreement with the experimental data[9,19]. Near the Γ point, one can observe a hexagonal-like shaped pocket of the spin-down states, which is to contribute to the nesting at wave vectors $\mathbf{q} = \mathbf{k} - \mathbf{k}'$ away from the zone center. Around the K points, one can see circular pockets allowing for transitions near the zone center i.e. at small $\mathbf{q}$. The spin-up (majority) Fermi surface is more complicated and it has more possibilities for transition at different $\mathbf{q}$. In both cases, the momentum transfer processes are expected to occur predominantly near the Γ point with discrete regions of $\mathbf{q}$ points around the nesting wave vectors. The electronic structure from the nonmagnetic calculations is considerably different. The Fermi surface is composed of circular pockets around the Γ point, allowing the transitions in a broad range of $\mathbf{q}$ vectors. We note that a moderate variation of the Fermi level (i.e. the doping effect) can significantly change the observed picture, which will influence the electron-phonon interaction as we will show below. It is also worth noting that the electronic states in monolayer Fe_3GeTe_2 are not strongly affected by the electron-phonon interactions. The spectral functions shown in the top of Fig. 2 do not show any significant renormalization in the vicinity of the Fermi energy in comparison to other systems[24]. At the same time, the inclusion of the electron-phonon coupling induces a finite linewidth, leading to a finite lifetime of charge carriers. The DOS calculated for the FM and nonmagnetic states, as well as in the disordered local moment approximation are presented in Supplementary Methods 2.

Phonon dispersion

The phonon dispersion and the corresponding spin-resolved linewidths are shown in Fig. 3 for the ferromagnetic and
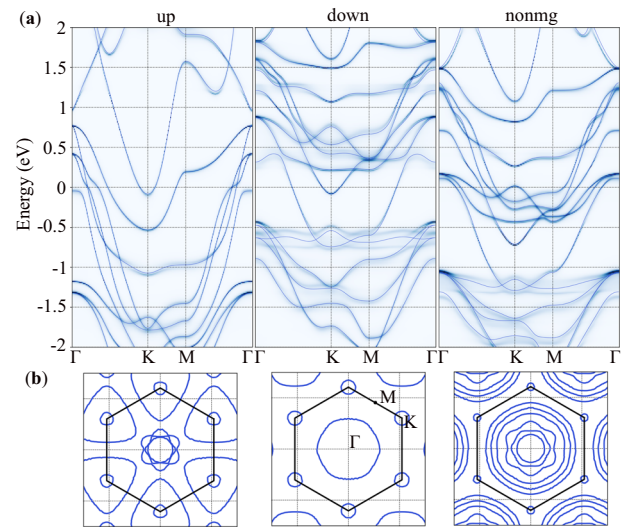

Fig. 2 Spin-dependent electron spectral functions and Fermi contour maps for the ferromagnetic and nonmagnetic phases of monolayer Fe_3GeTe_2. a Spectral functions $A_\mathbf{k}^\sigma(\omega, T) = -1/\pi \, \mathrm{Im}[G_\mathbf{k}^\sigma(\omega, T)]$ calculated in the presence of the electron-phonon interactions for $T = 100$ K for the states near the Fermi level. Original DFT band structure is shown by the blue solid line. Zero energy corresponds to the Fermi energy. **b** The corresponding Fermi contour maps.
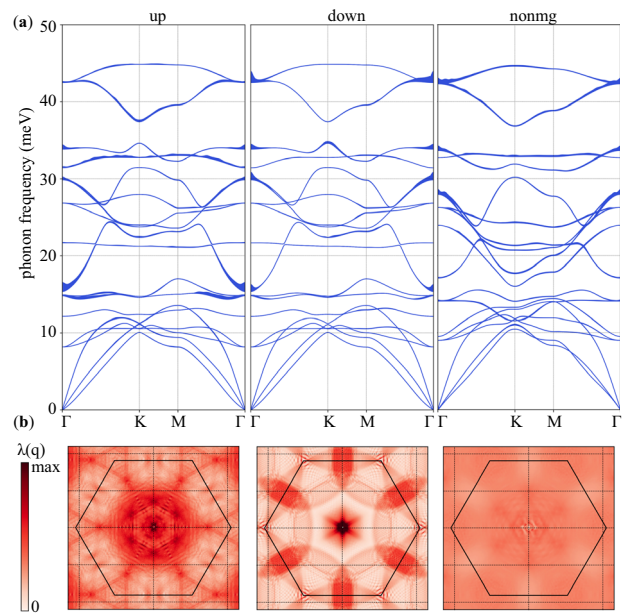

Fig. 3 Phonon dispersion curves and momentum-resolved electron-phonon coupling calculated for the ferromagnetic and nonmagnetic phases of monolayer Fe_3GeTe_2. a Phonon dispersion curves shown with the spin-dependent linewidth that is proportional to $\mathrm{Im}[\Pi_{\mathbf{q}\nu}^\sigma] = \pi N_F^\sigma \lambda_{\mathbf{q}\nu}^\sigma \omega_{\mathbf{q}\nu}^2$. **b** Momentum-resolved electron-phonon coupling constant $\lambda_\mathbf{q}^\sigma = \sum_\nu \lambda_{\mathbf{q}\nu}^\sigma$.

nonmagnetic calculations. The obtained dispersion of acoustic phonons is typical for 2D systems, demonstrating two linearly-dispersing branches and one flexural out-of-plane mode with a quadratic dispersion around the Γ point[24,26]. The optical phonon modes appear at energies from ~ 8 meV to ~ 45 meV. Interestingly, one can see a number of nearly flat branches, the most prominent of which appear near 15, 21, and 32 meV. The phonon modes with energies <15 meV correspond predominantly to the vibration of

heavy Te atoms, hybridized with Fe and Ge vibration states. The two highest energy modes represent a hybridized vibration of Fe and Ge atoms, while the rest phonon modes predominantly correspond to the Fe atoms vibration. Overall, the calculated phonon spectra are in good agreement with previously reported data[37]. The phonon linewidths are somewhat different for the magnetic and non-magnetic spectra. In particular, for the spin majority states in the ferromagnetic phase, most of the line broadening takes place near the Γ point around 15 meV, i.e. within the range of thermal excitations. In the nonmagnetic case, most of the line broadening is observed above 25 meV, thus their excitation is less likely. All this suggests that thermal transport in different magnetic states of FGT must be different, which might be interesting for further studies.

Electron-phonon coupling and its interpolation

We now turn to the electron-phonon interaction in monolayer Fe_3GeTe_2. As one can see from Fig. 3b, the **q**-resolved electron-phonon interaction constant $\lambda_\mathbf{q}$ is essentially different for spin-up and spin-down channels, which is expected from the spin-resolved linewidths shown above. For the spin-down states, the dominant electron-phonon coupling originates from the interaction with long-wavelength phonons, which results in a highly localized maximum of $\lambda_\mathbf{q}$ at the Γ point. In the spin-up case, the contributions with $\mathbf{q} > 0$ play a moderate role, although the maximum is still observed around the Γ point. In the nonmagnetic case $\lambda_\mathbf{q}$ is distributed practically uniformly, which is in line with the electronic structure and the Fermi contours discussed above.

The integrated electron-phonon coupling constant $\lambda^\sigma = \sum_{\mathbf{q}\nu} \lambda^\sigma_{\mathbf{q}\nu}$ for spin up and spin down states are found to be 0.50 and 0.26, respectively, i.e. $\lambda^\uparrow / \lambda^\downarrow \sim 2$. In the nonmagnetic case, we find $\lambda^{nonmg} \simeq 0.45$. The resulting constant $\lambda^\sigma < 1$, which can be qualified as a moderate electron-phonon interaction[38]. Given that the electron-phonon interaction constant is different for different magnetic states, it is important to take its temperature dependence into account when calculating the transport properties.

In what follows, we mimic the paramagnetic state of the system by a nonmagnetic solution obtained from the non-spin-polarized DFT calculations. Strictly speaking, this assumption is quite strong as it ignores the presence of residual disordered local magnetic moments at $T > T_C$, which may affect the electronic structure and related properties, especially in itinerant magnets. The most appropriate approach to deal with the paramagnetic state in first-principles calculations is to use the method of disordered local moments (DLM)[39–43]. This method requires considering large supercells in the DFT calculations, making DFPT calculations for paramagnetic states prohibitively expensive. However, our DLM calculations of the density of states (DOS) for monolayer Fe_3GeTe_2 (see Supplementary Methods 2) demonstrate that the DLM DOS near the Fermi energy turns out to be comparable to the nonmagnetic DOS. This behavior can be attributed to quenching of the local magnetic moment on the Fe_{II} atoms (see Fig. 1a) in most of the disordered configurations such that $\langle S_z^2 \rangle_{II} = 0$ in the DLM state. Unlike the ground-state FM configuration, the Fe_{II}-d states are not expected to be split in the paramagnetic phase, providing a sizeable contribution at the Fermi energy, as in the nonmagnetic solution.

Based on the argumentation given above, at temperatures $T > T_C$, we assume that the results converge to the nonmagnetic case. We can then approximate the temperature-dependent electron-phonon coupling constant using the interpolation formula:

$$\lambda^\sigma(T) = \lambda_{nonmg} + \left[\lambda^\sigma - \lambda_{nonmg}\right]\frac{\langle S_z \rangle}{S}. \tag{1}$$

At $T = 0$ K, the average spin $\langle S_z \rangle$ equals to the nominal spin $S = 1$, yielding $\lambda^\sigma(0) = \lambda^\sigma$. On the other hand, above Curie temperature, we have $\lambda^\sigma(T > T_C) = \lambda_{nonmg}$. The magnetization is determined self-consistently as described in Methods. The resulting magnetization curve is shown in Fig. 4, from which the Curie temperature
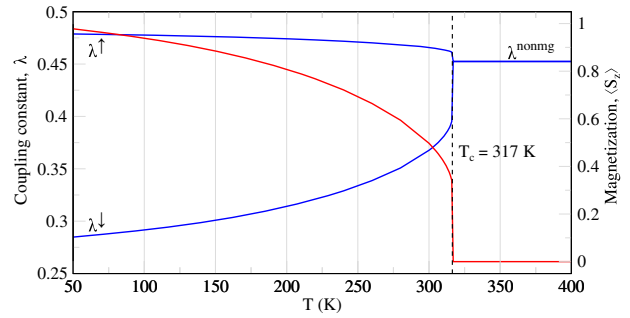

Fig. 4 Spin-resolved electron-phonon coupling constant λ^σ (blue) and magnetization $\langle S_z \rangle$ (red) calculated for monolayer Fe_3GeTe_2 as a function of temperature using the interpolation scheme discussed in the main text.

$T_C = 317$ K can be determined. The obtained value overestimates the experimental temperature $T_C \sim 200$ K[4,5,11,44] likely due to overestimation of the exchange interactions. This could be attributed to a limited applicability of the localized spin models, which neglect coupling to the electronic subsystem. In addition, renormalization of the electron spectrum due to correlation effects[9] may also contribute to the reduction of the exchange interactions. Also, the discrepancy between the theoretical and experimental T_C might be related, e.g., to contamination of the experimental samples, as well as to the effect of substrate, which is absent within our consideration. Nevertheless, the obtained magnetization curve $\langle S_z \rangle$ can be used to interpolate the results between the magnetic and nonmagnetic solutions keeping in mind that some ambiguity in the estimated T_C exists. In Fig. 4, we plot the result of the electron-phonon coupling constant interpolation using Eq. (1). With the increase of temperature the constants λ^σ for both spin channels smoothly change their values, converging into the nonmagnetic $\lambda_{nonmg} = 0.45$ result at T_C.

Temperature-dependent scattering rate

In Fig. 5a, we show averaged phonon-mediated scattering rate $\langle \tau_\sigma^{-1} \rangle = \frac{1}{N_F^\sigma} \sum_{n\mathbf{k}} \tau_{n\mathbf{k}\sigma}^{-1} \delta(\varepsilon_{n\mathbf{k}\sigma})$ as a function of temperature. Similarly to the coupling constant, the scattering rate calculated for the nonmagnetic phase has the value in between the spin-up and spin-down cases. At $T = 300$ K, we obtain $\langle \tau_\uparrow^{-1} \rangle = 117$ ps^{-1}, $\langle \tau_\downarrow^{-1} \rangle = 62$ ps^{-1}, and $\langle \tau_{nonmg}^{-1} \rangle = 91$ ps^{-1}. In the relevant temperature range, all these three curves demonstrate a linear-in-temperature behavior. Indeed, at sufficiently high temperatures phonons can be considered classically with the occupation numbers $b_{\mathbf{q}\nu} \simeq k_B T / \hbar \omega_{\mathbf{q}\nu}$, ensuring a linear dependence of the electron linewidth $\mathrm{Im}\Sigma_{\mathbf{q}\nu}^\sigma(T)$ as well as the scattering rate[26]. However, these results do not take temperature dependence of the electronic structure into account, which is important for magnetic systems. For this purpose, we use the following interpolation between the magnetic and nonmagnetic scattering rates

$$\left\langle \tau_\sigma^{-1}(T) \right\rangle = \left\langle \tau_{nonmg}^{-1} \right\rangle + \left[\left\langle \tau_\sigma^{-1} \right\rangle - \left\langle \tau_{nonmg}^{-1} \right\rangle\right]\frac{\langle S_z \rangle}{S}, \tag{2}$$

which allows us to make a connection between the scattering rates above and below T_C. The interpolation changes the linear dependence of $\langle \tau^{-1} \rangle$ at $T > 100$ K, inducing a convergence of $\langle \tau_\uparrow^{-1} \rangle$ and $\langle \tau_\downarrow^{-1} \rangle$ to the nonmagnetic solution $\langle \tau_{nonmg}^{-1} \rangle$ at $T = T_C$ (Fig. 5a). Remarkably, the averaged spin-up and spin-down scattering rates are very close the nonmagnetic scattering rate over the whole range of temperatures.

The magnon contribution to the scattering rate is shown in Fig. 5b. The electron-magnon coupling constant is estimated to be $I \cdot N_F \simeq 0.01$, i.e. an order of magnitude smaller compared to
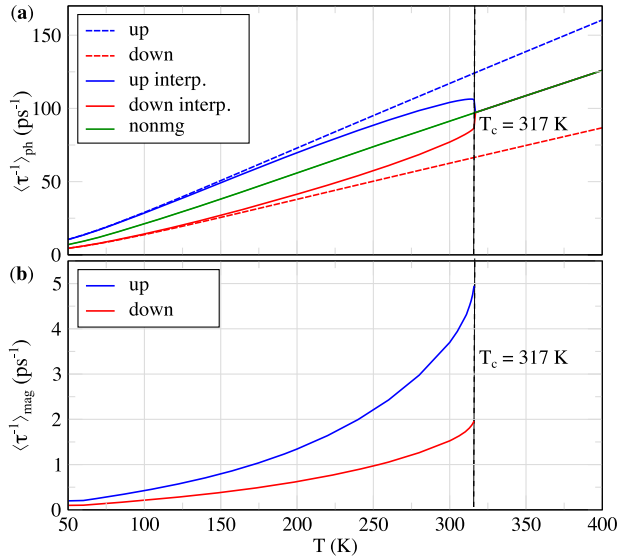
Fig. 5 Temperature-dependent electron-phonon and electron-magnon contributions to the scattering rate in monolayer Fe₃GeTe₂. a Averaged phonon-mediated scattering rate calculated for different spin channels in the ferromagnetic phase of monolayer Fe₃GeTe₂ (dashed lines), and for the nonmagnetic phase (green line). Solid red and blue lines correspond to the interpolation between the magnetic and nonmagnetic phases. **b** Averaged magnon-mediated scattering rate calculated for different spin channels.

the electron-phonon coupling. As a consequence, the calculated $\langle \tau^{-1} \rangle_{\text{mag}}$ is significantly smaller than $\langle \tau^{-1} \rangle_{\text{ph}}$ (Fig. 5b). Overall, the magnon-mediated scattering rate demonstrates an exponential increase with temperature up to T_C, which can be explained by the increase of the magnon population. Nevertheless, even close to T_C, the contribution of magnons to the scattering rate is marginal. At $T > T_C$ the long-range ferromagnetic order disappears, i.e. $\langle S_z \rangle = 0$, and Eq. (9) is seemingly inapplicable. However, the contribution of spin excitations does not disappear in the paramagnetic phase due to the short-range spin fluctuations[45]. Indeed, at sufficiently large T, we have $b_{\mathbf{q}\nu} \simeq k_B T / \hbar \omega_{\mathbf{q}\nu}$ with $\omega_{\mathbf{q}\nu} \sim \langle S_z \rangle$, leading to elimination of the magnetization in Eq. (9), which ensures nonzero scattering rate by static spin fluctuations. Nevertheless, as this contribution cannot be significantly larger than the contribution from magnons in the ferromagnetic phase, we ignore it from the explicit consideration.

Spin-resolved transport

We now calculate electric resistivity $\rho = 1/\sigma$ as a function of temperature by means of the semi-classical Boltzmann theory (Eq. (4) in Methods). To this end, we use the Matthiessen's rule[46], $\langle \tau^{-1} \rangle = \langle \tau_{\text{ph}}^{-1} \rangle + \langle \tau_{\text{mag}}^{-1} \rangle$. Fully spin-polarized (sp) resistivity ($\rho_{\text{sp}}^{-1} = \rho_{\uparrow}^{-1} + \rho_{\downarrow}^{-1}$) is represented in Fig. 6. Due to the magnon contribution, $\rho_{\text{sp}}(T)$ demonstrates a jump around T_C, which is attributed to the behavior of $\langle \tau_{\text{mag}}^{-1} \rangle$ shown in Fig. 5b.

The nonmagnetic resistivity ρ_{nonmg} demonstrates a less steep behavior compared to the resistivity in the ferromagnetic phase. This can be explained by the two factors: (i) temperature dependence of the scattering rate (Fig. 5); and (ii) different carrier velocities: $\bar{v}_{\uparrow,\downarrow} \simeq 2 \times 10^5$ m · s⁻¹, while $\bar{v}_{\text{nonmg}} = 1.3 \times 10^5$ m · s⁻¹. The interpolation of $\bar{v} \cdot N_F$ between the magnetic and nonmagnetic phases using the procedure described above, leads to the
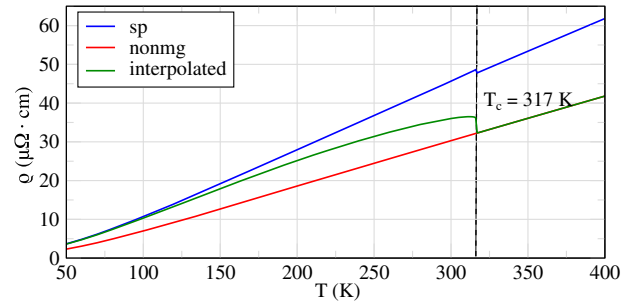

Fig. 6 Electrical resistivity shown as a function of temperature in monolayer Fe₃GeTe₂ calculated as: (i) $\rho_{\text{sp}}^{-1} = \rho_{\uparrow}^{-1} + \rho_{\downarrow}^{-1}$, i.e. from fully spin-polarized calculations without interpolation (low-T limit); (ii) ρ_{nonmg} i.e. nonmagnetic calculations ($T > T_C$); (iii) $\rho^{-1}(T) = \rho_{\uparrow}^{-1}(T) + \rho_{\downarrow}^{-1}(T)$ (interpolated via Eq.(3)).

following conductivity:

$$\sigma_\sigma(T) \simeq \frac{e^2}{\Omega} \langle \tau_\sigma(T) \rangle \langle \bar{v}_\sigma \cdot N_F^\sigma(T) \rangle, \tag{3}$$

which is shown as the green line in Fig. 6. One can see that at $T > 100$ K the linear resistivity behavior is modified, lowering the resistivity. At $T = T_C$ the resistivity drops abruptly to the nonmagnetic value. Such a behavior is likely unphysical and could be attributed to our approximation of the paramagnetic phase by a nonmagnetic one. Moreover, the transition region is to be smoothed by taking into account scattering by spin inhomogeneities above the Curie temperature as well as by the electron-impurity scattering. Nevertheless, our interpolated results allow us to qualitatively explain the temperature dependence of the resistivity near transition region observed in recent experiments[4,9,11,35,36].

At $T = 300$ K, the interpolated resistivity $\rho(T)$ is estimated to be 35 $\mu\Omega \cdot$ cm. The available experimental estimates for bulk FGT[4,9,11,35,36] vary from 150 to 200 $\mu\Omega \cdot$ cm, which is 4–5 times higher than the calculated values. This disagreement can be ascribed to the presence of other scattering channels in the experimental samples (e.g., impurities), which also leads to nonzero ρ at $T \sim 0$ K, as well as to the dimensionality effects. Our calculations provide the lowest boundary for the intrinsic resistivity in monolayer Fe₃GeTe₂. At the same time, this value is an order of magnitude larger than resistivities of noble metals such as $\rho_{\text{Cu}} \sim 1.5$ $\mu\Omega \cdot$ cm and $\rho_{\text{Au}} \sim 2.0$ $\mu\Omega \cdot$ cm[47]. The relatively high resistivity of monolayer FGT might limit its prospects for electronic applications.

DISCUSSION

In summary, we have systematically studied the charge-carrier scattering mechanisms in ferromagnetic monolayer Fe₃GeTe₂. We show that the phonon-mediated scattering of charge carriers plays a dominant role. The effect of magnons is also present, but can be considered as negligible in the relevant temperature region. At the same time, the magnetism-induced splitting of the energy bands modifies the electron-phonon coupling and induces a nontrivial contribution to its temperature dependence. This results in a sublinear temperature dependence of the electrical resistivity near the ferromagnetic-paramagnetic phase transition, observed experimentally. Also, we demonstrate that the charge doping (see Supplementary Methods 3) does not lead to any pronounced changes in the transport properties of Fe₃GeTe₂. Our calculations provide a lower estimate for the room temperature resistivity (35 $\mu\Omega \cdot$ cm) in monolayer FGT. The resulting value is an order of magnitude larger compared to typical metals, limiting potential applicability of monolayer FGT in electronics. For multilayer FGT, drastic changes of transport properties are not

expected due to comparably weak van der Waals interaction between the layers. Nevertheless, additional interlayer scattering may occur in multilayer samples, which would shorten the scattering rate. Therefore, in the absence of disorder, transport properties of monolayer FGT are expected to be superior to the multilayer samples. On the other hand, experimental single-layer samples are usually more contaminated compared to their multilayer counterparts, which might have an opposite effect on the layer-dependence of the transport properties.

The model approach presented in this paper to study transport properties of magnetic conductors can be applied to other 2D magnetic materials. Particularly, we expect a non-trivial role of the electron-magnon interactions in systems with weak electron-phonon coupling.

METHODS

Technical details

Electronic structure calculations and structural optimization were performed within the plane-wave based QUANTUM ESPRESSO (QE)[48,49] package utilizing Perdew-Burke-Ernzerhof (PBE) exchange-correlation functional[50] and 2.0.1 version scalar-relativistic norm-conserving pseudopotentials, generated using "atomic" code by A. Dal Corso v.5.0.99 svn rev. 10869. In these calculations, we use 80 Ry as the plane-wave energy cutoff, a $(16 \times 16 \times 1)$ **k**-mesh for the Brillouin zone integration, and 10^{-8} eV for the energy convergence criteria. The experimental crystal structure of bulk Fe_3GeTe_2 was used[3], where a vacuum space 20 Å between monolayer replicas in the vertical z direction was introduced to avoid spurious interactions between the periodic supercell images. The effective volume $\Omega = d \cdot S$ with layer thickness $d = 8.165$ Å of 2D unit cell area $S = 13.95$ Å^2 was used in the calculations. Positions of atoms were allowed to relax until all the residual force components of each atom were less than 10^{-4} eV $\cdot$ Å^{-1}. In the calculations of the transport properties we consider either the ferromagnetically ordered or nonmagnetic (non-spin-polarized) ground state. From the obtained electronic structure, maximally localized Wannier functions[51] were constructed using the WANNIER90 package[52] projecting onto the valence Fe(3d) and Te(5p) states, which were used in the calculations presented below. Phonon spectra were calculated using density functional perturbation theory (DFPT)[53] implemented in the QE package. In these calculations, we use a $(4 \times 4 \times 1)$ **q**−mesh and a 10^{-14} eV as the self-consistency threshold.

Electron transport

In the semi-classical Boltzmann theory, the in-plane (xx) component of the conductivity tensor has the form[46,54]:

$$\sigma_{xx}^{\sigma} = -\frac{e^2}{\Omega} \sum_{n\mathbf{k}} \frac{\partial f_{n\mathbf{k}}^{\sigma}}{\partial \varepsilon_{n\mathbf{k}}^{\sigma}} \tau_{n\mathbf{k}}^{\sigma} [v_{n\mathbf{k}\sigma}^{x}]^2, \tag{4}$$

with the momentum-dependent scattering rate $\tau_{n\mathbf{k}}$, which can be related to the imaginary part of the electron self-energy:

$$1/\tau_{n\mathbf{k}}^{\sigma} = \frac{2}{\hbar} \mathrm{Im} \Sigma_{n\mathbf{k}}^{\sigma}. \tag{5}$$

In the expression (4), $v_{n\mathbf{k}\sigma}^{x} = \partial \varepsilon_{n\mathbf{k}}^{\sigma} / \partial(\hbar k_x)$ is the x (in-plane) component of the group velocity for band n and wave-vector **k**, and $f_{n\mathbf{k}}^{\sigma}$ is the Fermi occupation function for the electron states with energy $\varepsilon_{n\mathbf{k}}^{\sigma}$, $f_{m\mathbf{k}}^{\sigma} = (\exp[(\varepsilon_{m\mathbf{k}}^{\sigma} - \varepsilon_{F})/k_B T] + 1)^{-1}$, where ε_F is the Fermi energy. We note that the expression (4) is applicable at not too low temperatures where vertex corrections, that is, difference between transport and single-electron relaxation time becomes important[27,46,54].

Phonon-mediated scattering was analyzed via calculating electron-phonon interaction. For this purpose, we use EPW[55] code, which takes the advantage of Wannier functions based

interpolation scheme[21]. Initial version of the code was modified to treat the spin channels independently. The electron self-energy of this interaction in the Migdal approximation has the following form:

$$\Sigma_{n\mathbf{k}}^{\sigma}(\omega, T) = \sum_{m\mathbf{q}\nu} |g_{mn,\nu}^{\sigma}(\mathbf{k}, \mathbf{q})|^2 \times$$

$$\times \left[\frac{b_{\mathbf{q}\nu} + f_{m\mathbf{k}+\mathbf{q}}^{\sigma}}{\omega - \varepsilon_{m\mathbf{k}+\mathbf{q}}^{\sigma} + \hbar\omega_{\mathbf{q}\nu} - i\eta} + \frac{b_{\mathbf{q}\nu} + 1 - f_{m\mathbf{k}+\mathbf{q}}^{\sigma}}{\omega - \varepsilon_{m\mathbf{k}+\mathbf{q}}^{\sigma} - \hbar\omega_{\mathbf{q}\nu} - i\eta} \right], \tag{6}$$

where $b_{\mathbf{q}\nu} = (\exp[\hbar\omega_{\mathbf{q}\nu}/k_B T] - 1)^{-1}$ corresponds to the Bose occupation function for phonons with wave vector **q**, mode index ν and frequency $\omega_{\mathbf{q}\nu}$. The electron-phonon matrix elements contain the information about the derivative of self-consisted spin dependent electronic potential $\partial_{\mathbf{q}\nu} V^{\sigma}$ in the basis of Bloch functions $\psi_{n\mathbf{k}}^{\sigma}$:

$$g_{mn,\nu}^{\sigma}(\mathbf{k}, \mathbf{q}) = \sqrt{\frac{\hbar}{2m_0\omega_{\mathbf{q}\nu}}} \langle \psi_{m\mathbf{k}+\mathbf{q}}^{\sigma} | \partial_{\mathbf{q}\nu} V^{\sigma} | \psi_{n\mathbf{k}}^{\sigma} \rangle. \tag{7}$$

The electron-phonon coupling constant for each phonon mode ν with wave vector **q** is given by

$$\lambda_{\mathbf{q}\nu}^{\sigma} = \frac{1}{N_F^{\sigma} \omega_{\mathbf{q}\nu}} \sum_{mn\mathbf{k}} |g_{mn,\nu}^{\sigma}(\mathbf{k}, \mathbf{q})|^2 \delta(\varepsilon_{n\mathbf{k}}^{\sigma}) \delta(\varepsilon_{m\mathbf{k}+\mathbf{q}}^{\sigma}), \tag{8}$$

where N_F^{σ} is the electron density of states (DOS) for spin σ at the Fermi level.

Magnon-mediated scattering is estimated from the electron-magnon interaction. The corresponding self-energy in case of a ferromagnetic order can be calculated in the spirit of the $s - d$ model[32–34] as:

$$\Sigma_{n\mathbf{k}}^{\uparrow}(\omega, T) = 2I^2 \langle S_z \rangle \sum_{\mathbf{q}\nu} \frac{b_{\mathbf{q}\nu} + f_{n\mathbf{k}+\mathbf{q}}^{\downarrow}}{\omega - \varepsilon_{n\mathbf{k}+\mathbf{q}}^{\downarrow} + \hbar\omega_{\mathbf{q}\nu} - i\eta}$$

$$\Sigma_{n\mathbf{k}}^{\downarrow}(\omega, T) = 2I^2 \langle S_z \rangle \sum_{\mathbf{q}\nu} \frac{b_{\mathbf{q}\nu} + 1 - f_{n\mathbf{k}-\mathbf{q}}^{\uparrow}}{\omega - \varepsilon_{n\mathbf{k}-\mathbf{q}}^{\uparrow} - \hbar\omega_{\mathbf{q}\nu} - i\eta}. \tag{9}$$

Here, I is the electron-magnon interaction constant ($s - d$ exchange parameter) averaged over the Fermi surface

$$I = \frac{1}{2SN_F} \sum_{m\mathbf{k}\sigma} (\varepsilon_{m\mathbf{k}}^{\uparrow} - \varepsilon_{m\mathbf{k}}^{\downarrow}) \frac{\partial f_{m\mathbf{k}}^{\sigma}}{\partial \varepsilon_{m\mathbf{k}}^{\sigma}}, \tag{10}$$

and $\langle S_z \rangle$ and $\omega_{\mathbf{q}\nu}$ correspond to the temperature-dependent magnetization and magnon frequencies, respectively. N_F is the total electron density of states at the Fermi energy, $N_F = N_F^{\uparrow} + N_F^{\downarrow}$. In both approximations [Eqs. (6) and (9)], we consider the static limit, i.e. $\omega = 0$ which is justifiable at not too low temperatures.

Temperature-dependent magnetization

In order to calculate $\langle S_z \rangle$ and $\omega_{\mathbf{q}\nu}$, we consider the following quantum spin model with $S = 1$:

$$\hat{\mathcal{H}} = \sum_{i>j} J_{ij} \hat{\mathbf{S}}_i \hat{\mathbf{S}}_j - A \sum_i S_{zi}^2. \tag{11}$$

The magnetic exchange interactions J_{ij} are calculated within the local force theorem approach[56,57] (see Supplementary Methods 1). We note that we are not aiming at a precise determination of the Hamiltonian parameters within this study which would require a complicated discussion on possible quantum corrections, etc. Our main purpose is to qualitatively reproduce the temperature-dependent magnetization as well as the magnon spectrum.

On-site anisotropy parameter $A = 0.35$ meV per Fe atom is calculated as a total energy difference for magnetic moments oriented along the in-plane and out-of-plane directions taking the spin-orbit coupling effects into account.

D.I. Badrtdinov et al.

Equation (11) allows us to introduce the spin-wave Hamiltonian, whose eigenvalues correspond to the magnon frequencies $\omega_{\mathbf{q}\nu}$[58]:

$$\hat{\mathcal{H}}_{\mu\nu}^{SW}(\mathbf{q}) = \left[\delta_{\mu\nu}\left[A + \sum_{\chi} J_{\mu\chi}(\mathbf{0})\right] - J_{\mu\nu}(\mathbf{q})\right]\langle S_z\rangle, \qquad (12)$$

where $J_{\mu\nu}(\mathbf{q})$ are the Fourier transform of the exchange interactions, and the indices μ and ν run from 1 to 3 over the Fe atoms in the unit cell.

In turn, the magnetization $\langle S_z\rangle$ entering Eq. (11) is calculated within the Tyablikov's Green's functions formalism[59,60]. The corresponding expression for $S = 1$ takes the form

$$\langle S_z\rangle = S\,\frac{1 + 2\sum_{\mathbf{q}\nu} b_{\mathbf{q}\nu}}{1 + 3\sum_{\mathbf{q}\nu} b_{\mathbf{q}\nu} + 3\left(\sum_{\mathbf{q}\nu} b_{\mathbf{q}\nu}\right)^2}. \qquad (13)$$

Here, the Bose factors $b_{\mathbf{q}\nu}$ depend on the magnon frequencies $\omega_{\mathbf{q}\nu}$, which are, in turn, obtained by diagonalizing the (3×3) Hamiltonian matrix [Eq. (12)]. In order to obtain $\langle S_z\rangle$ and $\omega_{\mathbf{q}\nu}$ simultaneously, we solve Eqs. (12) and (13) self-consistently. The resulting magnetization $\langle S_z\rangle$ drops down to zero at the Curie temperature T_C. Above this temperature the system becomes paramagnetic.

DATA AVAILABILITY

The data that support the findings of this work are available from the corresponding author upon reasonable request.

CODE AVAILABILITY

The central codes used in this paper are QUANTUM ESPRESSO[48,49], EPW[55] and WANNIER90[52] can be requested from developers.

REFERENCES

1. Huang, B. et al. Layer-dependent ferromagnetism in a van der Waals crystal down to the monolayer limit. *Nature* **546**, 270 (2017).
2. Gong, C. et al. Discovery of intrinsic ferromagnetism in two-dimensional van der Waals crystals. *Nature* **546**, 265 (2017).
3. Deiseroth, H.-J., Aleksandrov, K., Reiner, C., Kienle, L. & Kremer, R. K. Fe$_3$GeTe$_2$ and Ni$_3$GeTe$_2$ - two new layered transition-metal compounds: Crystal structures, HRTEM investigations, and magnetic and electrical properties. *Eur. J. Inorg. Chem.* **2006**, 1561 (2006).
4. Deng, Y. et al. Gate-tunable room-temperature ferromagnetism in two-dimensional Fe$_3$GeTe$_2$. *Nature* **563**, 94 (2018).
5. Fei, Z. et al. Two-dimensional itinerant ferromagnetism in atomically thin Fe$_3$GeTe$_2$. *Nat. Mater.* **17**, 778 (2018).
6. Li, Q. et al. Patterning-induced ferromagnetism of Fe$_3$GeTe$_2$ van der Waals materials beyond room temperature. *Nano Lett.* **18**, 5974 (2018).
7. Huang, B. et al. Electrical control of 2d magnetism in bilayer CrI$_3$. *Nat. Nanotechnol.* **13**, 544 (2018).
8. Soriano, D., Rudenko, A. N., Katsnelson, M. I. & Rösner, M. Environmental screening and ligand-field effects to magnetism in CrI$_3$ monolayer. *npj Comput. Mater.* **7**, 162 (2021).
9. Kim, K. et al. Large anomalous hall current induced by topological nodal lines in a ferromagnetic van der Waals semimetal. *Nat. Mater.* **17**, 794 (2018).
10. Roemer, R., Liu, C. & Zou, K. Robust ferromagnetism in wafer-scale monolayer and multilayer Fe$_3$GeTe$_2$. *npj 2D Mater. Appl.* **4**, 33 (2020).
11. Chen, B. et al. Magnetic properties of layered itinerant electron ferromagnet Fe$_3$GeTe$_2$. *J. Phys. Soc. Jpn.* **82**, 124711 (2013).
12. Laref, S., Kim, K.-W. & Manchon, A. Elusive Dzyaloshinskii-Moriya interaction in monolayer Fe$_3$GeTe$_2$. *Phys. Rev. B* **102**, 060402 (2020).
13. Ado, I. A., Rakhmanova, G., Zezyulin, D. A., Iorsh, I. & Titov, M. Quartic asymmetric exchange for two-dimensional ferromagnets with trigonal prismatic symmetry. *Phys. Rev. B* **106**, 144407 (2022).
14. Ding, B. et al. Observation of magnetic skyrmion bubbles in a van der Waals ferromagnet Fe$_3$GeTe$_2$. *Nano Lett.* **20**, 868 (2020).
15. Meijer, M. J. et al. Chiral spin spirals at the surface of the van der Waals ferromagnet Fe$_3$GeTe$_2$. *Nano Lett.* **20**, 8563 (2020).
16. Park, T.-E. et al. Néel-type skyrmions and their current-induced motion in van der Waals ferromagnet-based heterostructures. *Phys. Rev. B* **103**, 104410 (2021).
17. Müller, M. C. T. D., Blügel, S. & Friedrich, C. Electron-magnon scattering in elementary ferromagnets from first principles: lifetime broadening and band anomalies. *Phys. Rev. B* **100**, 045130 (2019).
18. Raquet, B., Viret, M., Sondergard, E., Cespedes, O. & Mamy, R. Electron-magnon scattering and magnetic resistivity in 3d ferromagnets. *Phys. Rev. B* **66**, 024433 (2002).
19. Zhang, Y. et al. Emergence of kondo lattice behavior in a van der Waals itinerant ferromagnet Fe$_3$GeTe$_2$. *Sci. Adv.* **4**, 6791 (2018).
20. Zhao, M. et al. Kondo holes in the two-dimensional itinerant ising ferromagnet Fe$_3$GeTe$_2$. *Nano Lett.* **21**, 6117 (2021).
21. Giustino, F. Electron-phonon interactions from first principles. *Rev. Mod. Phys.* **89**, 015003 (2017).
22. Poncé, S., Margine, E. R. & Giustino, F. Towards predictive many-body calculations of phonon-limited carrier mobilities in semiconductors. *Phys. Rev. B* **97**, 121201 (2018).
23. Sohier, T., Campi, D., Marzari, N. & Gibertini, M. Mobility of two-dimensional materials from first principles in an accurate and automated framework. *Phys. Rev. Mater.* **2**, 114010 (2018).
24. Lugovskoi, A. V., Katsnelson, M. I. & Rudenko, A. N. Strong electron-phonon coupling and its influence on the transport and optical properties of hole-doped single-layer inse. *Phys. Rev. Lett.* **123**, 176401 (2019).
25. Poncé, S., Li, W., Reichardt, S. & Giustino, F. First-principles calculations of charge carrier mobility and conductivity in bulk semiconductors and two-dimensional materials. *Rep. Prog. Phys.* **83**, 036501 (2020).
26. Rudenko, A. N. & Yuan, S. Electron-phonon interaction and zero-field charge carrier transport in the nodal-line semimetal zrsis. *Phys. Rev. B* **101**, 115127 (2020).
27. Katsnelson, M. I. *The Physics of Graphene* (Cambridge University Press, 2020).
28. Rudenko, A. N., Brener, S. & Katsnelson, M. I. Intrinsic charge carrier mobility in single-layer black phosphorus. *Phys. Rev. Lett.* **116**, 246401 (2016).
29. Fischetti, M. V. & Vandenberghe, W. G. Mermin-wagner theorem, flexural modes, and degraded carrier mobility in two-dimensional crystals with broken horizontal mirror symmetry. *Phys. Rev. B* **93**, 155413 (2016).
30. Rudenko, A. N. et al. Interplay between in-plane and flexural phonons in electronic transport of two-dimensional semiconductors. *Phys. Rev. B* **100**, 075417 (2019).
31. Nabok, D., Blügel, S. & Friedrich, C. Electron–plasmon and electron–magnon scattering in ferromagnets from first principles by combining gw and gt self-energies. *npj Comput. Mater.* **7**, 178 (2021).
32. Irkhin, V. Y. & Katsnelson, M. I. Kondo effect, spin dynamics and magnetism in anomalous rare earth and actinide compounds. *Zeitschrift für Physik B Condensed Matter* **75**, 67 (1989).
33. Katsnelson, M. I., Irkhin, V. Y., Chioncel, L., Lichtenstein, A. I. & de Groot, R. A. Half-metallic ferromagnets: From band structure to many-body effects. *Rev. Mod. Phys.* **80**, 315 (2008).
34. Irkhin, V. Y. & Irkhin, Y. P. *Electronic Structure, Correlation Effects and Physical Properties of d- and f-metals and Their Compounds* (Cambridge International Science Publishing, 2007).
35. Feng, H. et al. Resistance anomaly and linear magnetoresistance in thin flakes of itinerant ferromagnet Fe$_3$GeTe$_2$. *Chin. Phys. Lett.* **39**, 077501 (2022).
36. Liu, Y., Stavitski, E., Attenkofer, K. & Petrovic, C. Anomalous hall effect in the van der Waals bonded ferromagnet Fe$_{3-x}$GeTe$_2$. *Phys. Rev. B* **97**, 165415 (2018).
37. Zhuang, H. L., Kent, P. R. C. & Hennig, R. G. Strong anisotropy and magnetostriction in the two-dimensional stoner ferromagnet Fe$_3$GeTe$_2$. *Phys. Rev. B* **93**, 134407 (2016).
38. Allen, P. B. & Mitrović, B. *Theory of Superconducting T_C*, Solid State Physics, Vol. 37 (Academic Press, 1983).
39. Gyorffy, B. L., Pindor, A. J., Staunton, J., Stocks, G. M. & Winter, H. A first-principles theory of ferromagnetic phase transitions in metals. *J. Phys. F: Metal Phys.* **15**, 1337 (1985).
40. Staunton, J., Gyorffy, B. L., Pindor, A. J., Stocks, G. M. & .Winter, H. Electronic structure of metallic ferromagnets above the curie temperature. *J. Phys. F: Met. Phys.* **15**, 1387 (1985).
41. Pindor, A. J., Staunton, J., Stocks, G. M. & Winter, H. Disordered local moment state of magnetic transition metals: a self-consistent KKR CPA calculation. *J. Phys. F: Met. Phys.* **13**, 979 (1983).
42. Staunton, J., Gyorffy, B. L., Stocks, G. M. & Wadsworth, J. The static, paramagnetic, spin susceptibility of metals at finite temperatures. *J. Phys. F: Met. Phys.* **16**, 1761 (1986).
43. Niklasson, A. M. N. et al. Modeling the actinides with disordered local moments. *Phys. Rev. B* **67**, 235105 (2003).

44. Verchenko, V. Y., Tsirlin, A. A., Sobolev, A. V., Presniakov, I. A. & Shevelkov, A. V. Ferromagnetic order, strong magnetocrystalline anisotropy, and magnetocaloric effect in the layered telluride $Fe_{3-\delta}GeTe_2$. *Inorg. Chem.* **54**, 8598 (2015).

45. Fisher, M. E. & Langer, J. S. Resistive anomalies at magnetic critical points. *Phys. Rev. Lett.* **20**, 665 (1968).

46. Ziman, J. *Electrons and Phonons: The Theory of Transport Phenomena in Solids* (Oxford University Press, Oxford, England, 2001).

47. Mustafa, J. I., Bernardi, M., Neaton, J. B. & Louie, S. G. Ab initio electronic relaxation times and transport in noble metals. *Phys. Rev. B* **94**, 155105 (2016).

48. Giannozzi, P. et al. Quantum espresso toward the exascale. *J. Chem. Phys.* **152**, 154105 (2020).

49. Giannozzi, P. et al. Advanced capabilities for materials modelling with quantum ESPRESSO. *J. Phys. Condens. Matter.* **29**, 465901 (2017).

50. Perdew, J. P., Burke, K. & Ernzerhof, M. Generalized gradient approximation made simple. *Phys. Rev. Lett.* **77**, 3865 (1996).

51. Marzari, N. & Vanderbilt, D. Maximally localized generalized Wannier functions for composite energy bands. *Phys. Rev. B* **56**, 12847 (1997).

52. Pizzi, G. et al. Wannier90 as a community code: new features and applications. *J. Phys. Condens. Matter.* **32**, 165902 (2020).

53. Baroni, S., de Gironcoli, S., Dal Corso, A. & Giannozzi, P. Phonons and related crystal properties from density-functional perturbation theory. *Rev. Mod. Phys.* **73**, 515 (2001).

54. Ziman, J. M. *Principles of the Theory of Solids* (Cambridge University Press, Cambridge, England, 1964).

55. Poncé, S., Margine, E., Verdi, C. & Giustino, F. Epw: Electron-phonon coupling, transport and superconducting properties using maximally localized wannier functions. *Comput. Phys. Commun.* **209**, 116 (2016).

56. Liechtenstein, A. I., Katsnelson, M. I., Antropov, V. P. & Gubanov, V. A. Local spin density functional approach to the theory of exchange interactions in ferromagnetic metals and alloys. *J. Magn. Magn. Mater.* **67**, 65 (1987).

57. Kashin, I. V., Mazurenko, V. V., Katsnelson, M. I. & Rudenko, A. N. Orbitally-resolved ferromagnetism of monolayer CrI_3. *2D Mater.* **7**, 025036 (2020).

58. Rusz, J., Turek, I. & Diviš, M. Random-phase approximation for critical temperatures of collinear magnets with multiple sublattices: GdX compounds ($X =$ Mg, Rh, Ni, Pd). *Phys. Rev. B* **71**, 174408 (2005).

59. Tyablikov, S. V. *Methods in Quantum Theory of Magnetism* (Springer, New York, 1983).

60. Nolting, W. & Ramakanth, A. *Quantum Theory of Magnetism* (Springer-Verlag, Berlin, Heidelberg, 2009).

ACKNOWLEDGEMENTS

AUTHOR CONTRIBUTIONS

All Authors discussed the results and contributed to the preparation of the manuscript.

COMPETING INTERESTS

The authors declare no competing interests.

ADDITIONAL INFORMATION

Supplementary information The online version contains supplementary material available at https://doi.org/10.1038/s41699-023-00413-0.

Correspondence and requests for materials should be addressed to Danis I. Badrtdinov or Alexander N. Rudenko.

Reprints and permission information is available at http://www.nature.com/reprints

Publisher's note Springer Nature remains neutral with regard to jurisdictional claims in published maps and institutional affiliations.